

Contribution of the first galaxies to the cosmic far-infrared/sub-millimeter background – I. Mean background level

María Emilia De Rossi^{1,2*} and Volker Bromm³

¹ *Consejo Nacional de Investigaciones Científicas y Técnicas, Argentina*

² *Instituto de Astronomía y Física del Espacio (IAFE, CONICET-UBA), CC 67, Suc. 28, 1428 Buenos Aires, Argentina*

³ *Department of Astronomy, University of Texas at Austin, 2511 Speedway, Austin, TX 78712, USA*

Accepted ????. ??, 2016

ABSTRACT

We study the contribution of the first galaxies to the far-infrared/sub-millimeter (FIR/sub-mm) extragalactic background light (EBL) by implementing an analytical model for dust emission. We explore different dust models, assuming different grain size distributions and chemical compositions. According to our findings, observed re-radiated emission from dust in dwarf-size galaxies at $z \sim 10$ would peak at a wavelength of $\sim 500\mu\text{m}$ with observed fluxes of $\sim 10^{-3} - 10^{-2}$ nJy, which is below the capabilities of current observatories. In order to be detectable, model sources at these high redshifts should exhibit luminosities of $\gtrsim 10^{12}L_{\odot}$, comparable to that of local ultra-luminous systems. The FIR/sub-mm EBL generated by primeval galaxies peaks at $\sim 500\mu\text{m}$, with an intensity ranging from $\sim 10^{-4}$ to $10^{-3}\text{ nW m}^{-2}\text{ sr}^{-1}$, depending on dust properties. These values are $\sim 3 - 4$ orders of magnitude below the absolute measured cosmic background level, suggesting that the first galaxies would not contribute significantly to the observed FIR/sub-mm EBL. Our model EBL exhibits a strong correlation with the dust-to-metal ratio, where we assume a fiducial value of $D = 0.005$, increasing almost proportionally to it. Thus, measurements of the FIR/sub-mm EBL could provide constraints on the amount of dust in the early Universe. Even if the absolute signal from primeval dust emission may be undetectable, it might still be possible to obtain information about it by exploring angular fluctuations at $\sim 500\mu\text{m}$, close to the peak of dust emission from the first galaxies.

Key words: cosmology: theory – galaxies: evolution – galaxies: abundances – galaxies: haloes – galaxies: high-redshift – galaxies: star formation

1 INTRODUCTION

The emergence of the first stellar systems fundamentally transformed the Universe from its simple initial state during the cosmic dark ages into one of progressively larger complexity (e.g. Barkana & Loeb 2001; Loeb 2010). Besides contributing to the reionization of the Universe, primordial stars enriched the pristine gas with the first heavy chemical elements (e.g. Bromm & Loeb 2003; Furlanetto & Loeb 2003; Yoshida, Bromm & Hernquist 2004), including the formation of dust (Schneider et al. 2006; Cherchneff & Dwek 2010; Chiaki et al. 2015). The complex physics of pre-galactic metal enrichment (e.g. Karlsson, Bromm & Bland-Hawthorn 2013), and the prop-

erties of primordial dust inside the first cosmic structures (e.g. Loeb & Haiman 1997; Schneider, Ferrara & Salvaterra 2004; Gall, Hjorth & Andersen 2011) constitute frontier topics in modern cosmology as they are concerned with the foundation for subsequent galaxy formation.

Within the standard Λ -Cold Dark Matter (Λ CDM) model, the first stellar populations are predicted to have formed from metal-free gas inside dark matter minihaloes ($\sim 10^6 M_{\odot}$) at $z \gtrsim 20$ (e.g. Couchman & Rees 1986; Haiman, Thoul & Loeb 1996; Tegmark et al. 1997; Yoshida et al. 2003; Bromm & Larson 2004; Bromm et al. 2009; Bromm 2013a). The first stars, the so-called Population III (Pop III), exhibited high characteristic masses ($\sim 10 - 100 M_{\odot}$), and had correspondingly short lifetimes (e.g. Abel, Bryan & Norman 2002; Bromm, Coppi & Larson 2002; Stacy, Greif & Bromm

* Email:mariaemilia.dr@gmail.com

2010; Greif et al. 2011). Pop III stars, therefore, may have been important sources of dust at early epochs. Owing to the shallow gravitational potential wells of minihaloes, the strong negative feedback from Pop III stars probably heated and expelled all remaining gas, inhibiting further star formation (SF). This implies that Pop III minihaloes would not have been true galaxies, if they are defined as the hosts of long-lived stellar systems. The deeper potential wells of atomic cooling haloes, with virial masses of $\sim 10^7 - 10^8 M_\odot$, are promising candidates for hosting second-generation metal-poor (Pop II) stars at $z \sim 20 - 6$ (Bromm & Yoshida 2011; Bromm 2013b). Hence, these systems would be the first protogalaxies in the pre-reionization Universe. At this epoch, the SF process transitioned into a low-mass dominated mode, described by a more normal initial mass function (IMF), similar to the near-universal Salpeter law (e.g. Frebel, Johnson & Bromm 2007; Ji, Frebel & Bromm 2014). This transition was likely driven by a combination of atomic fine structure cooling and dust thermal emission. Thus, the first galaxies might have been composed of Pop II stellar systems, surrounded by a mixed phase of gas and dust inside atomic cooling haloes.

In modern cosmology, a challenging issue is to understand the interconnection between the diffuse Extragalactic Background Light (EBL) and the first luminous systems, specifically to determine to what extent this radiation could be attributed to sources in the early Universe. Primordial stellar populations are expected to have left a measurable imprint on the absolute optical and near-infrared (NIR, $\lambda \sim 1 - 10 \mu\text{m}$) EBL (e.g. Santos, Bromm & Kamionkowski 2002), and its spatial fluctuations (e.g. Cooray et al. 2004; Kashlinsky et al. 2004). As photons propagate towards the observer in an expanding Universe, they lose energy and any radiation associated with the first stellar systems will be seen mostly in the NIR (Bromm 2013a), peaking at about $1 \mu\text{m}$. In particular, HII regions enclosing ionizing sources in the first luminous systems contribute to the cosmic near-infrared background by redshifted Lyman- α emission (e.g. Salvaterra & Ferrara 2003). On the other hand, UV radiation from primordial stars that heated interstellar dust and was re-radiated at longer wavelengths contributed to the EBL in the far-IR/sub-millimeter (FIR/sub-mm) part of the spectrum (e.g. Low & Tucker 1968; Kaufman 1976; Carr, Bond & Arnett 1984; Beichman & Helou 1991; Dwek et al. 1998).

The origin of the NIR-EBL, often succinctly referred to as the “cosmic infrared background” (CIB), has been widely discussed in the literature. Specifically, the measured excess in the NIR-EBL over what is expected from known galaxies might be indicating a significant contribution from early epochs (e.g. Kashlinsky 2005). However, because of the difficulties to measure absolute flux due to the strong foregrounds, CIB studies have mainly focused on the determination of spatial fluctuations. Recently, Mitchell-Wynne et al. (2015) performed a multiwavelength study by using one of the deepest surveys with the Hubble Space Telescope. In analysing CIB spatial fluctuation at $\lambda = 0.6 - 1.6 \mu\text{m}$, they infer a significant surface density of faint sources at $z > 8$, which are still below the point-source sensitivities of current observatories. This result is encouragingly consistent to previous findings deduced by Kashlinsky et al. (2007) by using *Spitzer* data. With the advent of new instruments such as

the NIRCam on the *James Webb Space Telescope* (JWST), the detection of individual, fainter systems will become possible, resolving the sources of the CIB to even higher z .

With respect to the FIR/sub-mm EBL, observational studies benefit from the negative K-correction. Sources associated with this wavelength range are generally dusty galaxies, where surrounding dust absorbs optical/UV emission from young stars, to be re-radiated in the FIR. During the last two decades, the SCUBA and LABOCA surveys resolved 20-40% of the EBL at $850 \mu\text{m}$ (e.g. Eales et al. 2000; Coppin et al. 2006; Weiß et al. 2009), and 10-20% at 1 mm in deep surveys with the AzTEC camera (Wilson et al. 2008). In recent years, it was suggested that bright dusty high- z sub-mm galaxies (SMGs; Casey, Narayanan & Cooray 2014) can account for more than half of the EBL at $850 \mu\text{m}$ (Viero et al. 2013; Cai et al. 2013). However, SMGs constitute an extreme case and cannot be representative of the bulk of the galaxy population at high z . The major contribution to the observed flux at mm/sub-mm wavelengths seems to originate in fainter ($< 1 \text{ mJy}$), high- z populations different from SMGs. Very recently, the higher sensitivity of the Atacama Large Millimeter/submillimeter Array (ALMA) allows to infer the number counts at fluxes fainter than 1 mJy. Hatsukade et al. (2013) resolved 80% of the EBL at 1.3 mm, when exploring faint (0.1-1 mJy) objects. Similar findings were reported by Ono et al. (2014) at 1.2 mm. In addition, Carniani et al. (2015) identified 50 sources down to $60 \mu\text{Jy}$, claiming that the observed flattening of the integrated number counts at faint fluxes might be indicating that they are close to resolving 100% of the cosmic background, subject to large uncertainties regarding the absolute EBL level.

Although the contribution of the first stellar systems to the NIR-EBL has been extensively studied (e.g. Santos, Bromm & Kamionkowski 2002; Salvaterra & Ferrara 2003, 2006; Kashlinsky et al. 2002, 2004, 2005; Magliocchetti, Salvaterra & Ferrara 2003; Cooray et al. 2004; Cooray & Yoshida 2004), their role as possible FIR/sub-mm sources is still poorly explored. In this paper, we ask to what extent the first galaxies may have contributed to the observed FIR/sub-mm EBL through redshifted dust re-emission. To accomplish this, we implement an idealized analytical model designed to reproduce properties of the first galactic systems. This model is then combined with a Sheth-Tormen halo mass function to estimate their contribution to the EBL at FIR/sub-mm wavelengths.

In Section 2, we discuss our primeval galaxy models in detail, to be followed in Section 3 and 4 with the description of our background light modelling. We conclude in Section 5 with a brief outlook into future developments. The following cosmological parameters are assumed in this work: $h = 0.67$, $\Omega_b = 0.049$, $\Omega_M = 0.32$, $\Omega_\Lambda = 0.68$ (Planck Collaboration et al. 2014).

2 DUST EMISSION FROM PRIMEVAL GALAXIES

We developed an idealized model to explore dust emission signatures associated with haloes hosting the first Pop II stellar populations. Observed specific fluxes were calculated

for individual sources of different masses and at different redshifts. In Section 3, we will combine these models with the Sheth-Tormen halo mass function to predict the observed cosmic background in the FIR/sub-mm range. We now proceed to describe the model and our choice of input parameters.

2.1 Model galaxies

We consider the idealized case of a dark-matter halo hosting a central stellar cluster, surrounded by a mixed phase of gas and dust that extends towards the virial radius (R_{vir}). We assume spherical symmetry inside these systems, and do not consider any extended distribution of halo stars. To construct the density profile for the *gaseous* component, we adopt an isothermal power law of the form $\sim r^{-2}$, as it provides a good description of a virialized system (Binney & Tremaine 2008). Following Smith et al. (2015), we consider a non-cuspy ‘core’, consistent with observations of low surface brightness galaxies (e.g. Kormendy et al. 2009). Thus, the gas mass density profile has the form:

$$\rho_g(r) \propto \begin{cases} 1 & r \leq R_c \\ (\frac{R_c}{r})^2 & R_c < r \leq R_{\text{vir}} \end{cases} \quad (1)$$

where R_c denotes a ‘core’ radius within which the density flattens off to a constant value. By construction, this density profile satisfies the following condition:

$$1 < F_g = \frac{M_{\text{vir,g}}}{\frac{4}{3}\pi R_{\text{vir}}^3 \rho_g(r=R_{\text{vir}})} < 3. \quad (2)$$

where $M_{\text{vir,g}}$ is the total gas mass contained inside R_{vir} .

For a given halo virial mass (M_{vir}) and redshift (z), R_{vir} is defined as the radius which encloses an overdensity of 200 with respect to the cosmic mean, $\bar{\rho}(z)$, at that redshift (Bromm 2013b). The parameter R_c and the central gas density are set by imposing two additional conditions. Firstly, for the baryon-to-total mass ratio of the system to be of order the cosmic mean Ω_b/Ω_M , we require that $\rho_g(R_{\text{vir}}) = 200(\Omega_b/\Omega_M)\bar{\rho}(z)$. We are assuming that the stellar contribution is negligible, which should be valid for the first galaxies. Secondly, we fix F_g in such a way that central gas densities are consistent with the expectation for the first galaxies ($\gtrsim 1 \text{ cm}^{-3}$), resulting in $F_g \approx 2.8$. By construction, in this model, central densities are similar at similar redshifts, regardless of halo mass. For our selected parameters, they range from $n_g \sim 2.0 \text{ cm}^{-3}$ at $z = 7$ to $n_g \sim 40 \text{ cm}^{-3}$ at $z = 20$. In Fig. 1, we show sample density profiles for systems of different mass at $z = 10$. We derive the dust density distribution inside haloes from the gas density by assuming a dust-to-metal mass ratio $D = M_d/M_Z = 5 \times 10^{-3}$, and a gas metallicity of $Z_g = 5 \times 10^{-3} Z_\odot$.¹

As our model galaxies include a primordial dust component, their stellar populations should have already been enriched with metals. For simplicity, we assume that a compact cluster of Pop II stars resides in the center of the host

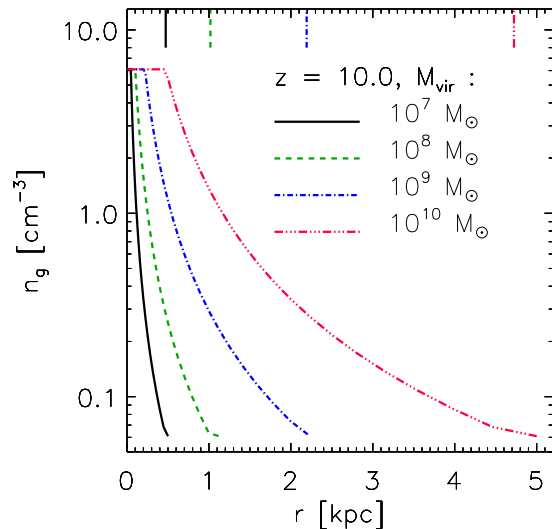


Figure 1. Gas density profiles for model galaxies with different M_{vir} at $z = 10$. The vertical lines on the top depict the virial radii of these systems. Note that the vertical axis employs logarithmic scaling.

halo, modelled subsequently as a point source of stellar radiation. The cluster is assumed to have been formed during a single instantaneous burst following a Kroupa (2001) IMF, which is a good approximation for Pop II stars inside the first galaxies (Safranek-Shrader, Bromm & Milosavljević 2010; Safranek-Shrader, Milosavljević & Bromm 2014). In order to estimate its total stellar mass (M_*), we assign a star formation efficiency of $\eta = M_*/(M_g + M_*) = 0.01$ to the system (Greif & Bromm 2006; Mitchell-Wynne et al. 2015). We construct the spectral energy distribution (SED) associated with this system using Yggdrasil model grids (Zackrisson et al. 2011). Specifically, we adopt models corresponding to their lowest available stellar metallicity, $Z_* \approx 3 \times 10^{-2} Z_\odot$, and a stellar age $\tau = 0.01 \text{ Myr}$. In this case, Yggdrasil employs SEDs derived from Starburst99 single stellar population (SSP) models, based on Padova asymptotic giant branch (AGB) tracks (Leitherer et al. 1999; Vázquez & Leitherer 2005), with a Kroupa IMF in the interval $0.1\text{--}100 M_\odot$.

2.2 Dust model

In modelling the dust chemical composition and grain size distribution, we follow Ji, Frebel & Bromm (2014), who considered a suite of different silicon-based dust models (see table 1 in Ji, Frebel & Bromm 2014), calculated by Cherchneff & Dwek (2010): UM-ND-20, UM-ND-170, UM-D-20, UM-D-170, M-ND-20, M-ND-170, M-D-20 and M-D-170.² As in Ji, Frebel & Bromm (2014), we will not try to address which prescription is more realistic and take all

¹ We adopt $Z_\odot = 0.0127$ (Allende Prieto, Lambert & Asplund 2001), which corresponds to the default in CLOUDY (version 07.02, Ferland et al. 1998). This value is also consistent with that reported by Asplund, Grevesse & Sauval (2005, $Z_\odot = 0.0122$) and, more recently, by Asplund et al. (2009, $Z_\odot = 0.0134$).

² Model names refer to the type of dust model from Cherchneff & Dwek (2010): UM = unmixed, M = mixed; ND = non depleted, D = depleted; 170: 170 M_\odot progenitor, 20: 20 M_\odot progenitor.

of them as plausible variations in the chemical composition of dust. Representative species in these models are SiO_2 , Mg_2SiO_4 , amorphous Si, and FeS. It is worth mentioning that Cherchneff & Dwek (2010) estimated dust chemistry considering non-equilibrium chemical kinetics for dust formation; instead, most steady-state models would predict a dominant carbon dust composition. In addition, in the context of the Cherchneff & Dwek (2010) models, the suppression of carbon dust relies on the hypothesis that carbon-rich regions in the supernova ejecta are microscopically mixed with helium ions. We here follow these assumptions, but we acknowledge that there is an ongoing debate about the extent to which carbon dust formation is inhibited (e.g. Nozawa & Kozasa 2013). However, our overall conclusions would remain valid also for a dust composition that contains a carbon-based component as well.

For the grain size distribution, we consider the simple, well-motivated “standard” prescription of Pollack et al. (1994). This was used in Omukai, Hosokawa & Yoshida (2010), and it is similar to the Milky Way grain size distribution used in, e.g., Dopcke et al. (2013). For spherical dust grains of radius a , the distribution is:

$$\frac{dn_{\text{standard}}}{da} \propto \begin{cases} 1 & a < 0.005\mu\text{m} \\ a^{-3.5} & 0.005\mu\text{m} < a < 1\mu\text{m} \\ a^{-5.5} & 1\mu\text{m} < a < 5\mu\text{m} \end{cases} . \quad (3)$$

We also explored the shock size distribution used by Ji, Frebel & Bromm (2014):

$$\frac{dn_{\text{shock}}}{da} \propto \begin{cases} 1 & a < 0.005\mu\text{m} \\ a^{-5.5} & a > 0.005\mu\text{m} \end{cases} . \quad (4)$$

The latter distribution approximates the effect of running a post-supernova reverse shock through newly created dust and is based on the work of Bianchi & Schneider (2007). For simplicity, each type of dust grain is assumed to have the same grain size distribution. These models for dust chemistry and grain sizes are then used to obtain dust geometrical cross sections and dust opacities as described in Ji, Frebel & Bromm (2014), and we refer the reader to that paper for details.

2.2.1 Dust temperature profile

To determine the dust temperature (T_d), we assume thermal equilibrium. We set the dust cooling rate, $\Lambda_d(T_d)$, equal to the dust heating rate driven by gas-dust collisions, H_d , and by the stellar-source radiation, H_* . As discussed below, because of the low interstellar medium (ISM) densities of our model galaxies, H_* constitutes generally the dominant heating term. The cosmic microwave background (CMB) provides a temperature floor, T_{CMB} , because it is thermodynamically not possible to radiatively cool below. Thus, the basic equation to be solved is:

$$\Lambda_d(T_d) - \Lambda_d(T_{\text{CMB}}) = H_d + H_* . \quad (5)$$

The procedure to estimate Λ_d and H_d is similar to that in Ji, Frebel & Bromm (2014), and we briefly describe it here for the convenience of the reader, also noting that the calculation of Λ_d closely follows the methodology in Schneider et al. (2006).

Dust grain emission is well approximated by thermal radiation (Draine & Li 2001), in which case the cooling rate can be written

$$\Lambda_d(T_d) = 4\sigma_{\text{SB}}T_d^4\kappa_{\text{P,d}}\rho_d\beta_{\text{esc}} , \quad (6)$$

where σ_{SB} is the Stefan-Boltzmann constant, $\kappa_{\text{P,d}}$ the temperature-dependent Planck mean opacity of dust grains per unit *dust* mass, ρ_d the dust mass density, and β_{esc} the photon escape probability. For the Planck dust opacities, we use the tabulated values derived by Ji, Frebel & Bromm (2014), kindly provided by Alexander Ji (private communication). The escape fraction is estimated as $\beta_{\text{esc}} = \min(1, \tau^{-2})$, which is suitable for radiative diffusion out of an optically thick gas cloud (Omukai 2000). The optical depth τ is given by:

$$\tau = (\kappa_{\text{P,g}}\rho_g + \kappa_{\text{P,d}}\rho_d)\lambda_J , \quad (7)$$

where $\kappa_{\text{P,g}}$ is the continuum Planck mean opacity of primordial gas from Mayer & Duschl (2005), and λ_J the Jeans length. The Jeans length is the typical size of a dense core in a uniformly collapsing spherical gas cloud (e.g. Larson 1969). For the densities encountered in this work, $\beta_{\text{esc}} \approx 1$ provides a good approximation.

The gas-dust collisional heating rate (Hollenbach & McKee 1979) is computed as:

$$H_d = nn_d\sigma_d v_{\text{th}} f(2k_B T_g - 2k_B T_d) , \quad (8)$$

where n is the number density of atomic hydrogen, n_d the number density of dust, σ_d the dust geometrical cross section, v_{th} the thermal velocity of atomic hydrogen, T_g the gas temperature, and f is a correction factor for species other than atomic hydrogen. Note that $n_d\sigma_d = \rho_d S$, where S , the total dust geometrical cross section per unit dust mass, is defined as:

$$S = \sum_i f_i S_i \text{ with } S_i = \int_0^\infty \pi a^2 \frac{dn_i}{da} da , \quad (9)$$

with f_i denoting the mass fraction, and the sum extending over the respective species considered in a given model. Since higher energy particles collide more frequently (Draine 2011), the kinetic energy per colliding gas particle is $2k_B T$ instead of $1.5k_B T$. A Maxwellian velocity distribution is adopted for the gas so the average velocity of atomic hydrogen is

$$v_{\text{th}} = \left(\frac{8k_B T_g}{\pi m_H} \right)^{1/2} . \quad (10)$$

Finally, for obtaining the dust heating rate driven by stellar radiation, we estimate the specific flux emerging from the central source, $f_{*,\nu}$, that is absorbed by dust grains at a given radius r . For simplicity, we assume isotropic emission and negligible extinction between the stellar source and dust grains (optically thin medium). Hence,

$$f_{*,\nu} = \frac{L_{*,\nu}}{4\pi r^2} , \quad (11)$$

where $L_{*,\nu}$ is the specific luminosity of the stellar cluster, modelled as a point source. The stellar luminosity is derived by rescaling Yggdrasil SEDs to the mass of the central cluster. Thus,

$$H_* = \int_0^\infty \kappa_\nu \rho_d f_{*,\nu} d\nu , \quad (12)$$

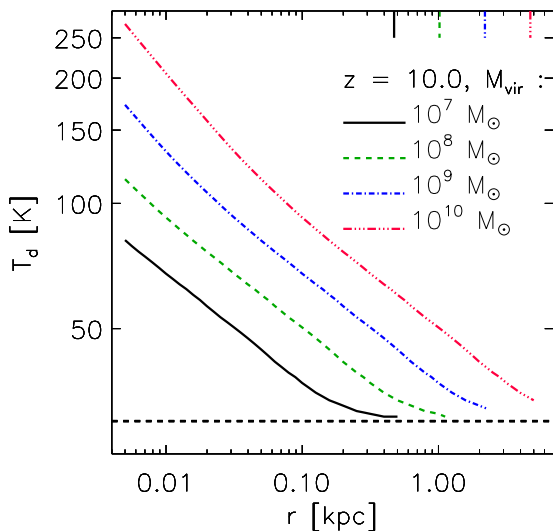


Figure 2. Dust temperature profiles for the same systems shown in Fig. 1, generated by assuming the UM-ND-20 dust model and standard size distribution for dust grains (see text for details). The vertical lines on the top again depict the virial radii of these systems. The horizontal dashed line denotes the CMB temperature at $z = 10$. Note that temperatures are higher in the more massive systems, since the luminosity of the central star cluster is scaled up accordingly.

with κ_ν representing the frequency-dependent dust opacity per unit mass calculated by Ji, Frebel & Bromm (2014).

Inside atomic cooling haloes, T_g is expected to range between $\sim 10^2$ and 10^4 K, depending on the physical condition of the gas phase (e.g. Safranek-Shrader, Bromm & Milosavljević 2010; Safranek-Shrader, Milosavljević & Bromm 2014). However, because of the low density of the gas component encountered in this work, our results indicate that T_d is not very sensitive to variations in T_g . We verified this for all systems considered here, specifically for $M_{\text{vir}} \geq 10^7 M_\odot$ and $z \in [7, 20]$, by assuming an isothermal gas component with three different values of T_g : $10^2, 10^3, 10^4$ K. We obtained, in all cases, similar values of T_d because the stellar heating rate dominates over that driven by gas-dust collisions: $H_d/H_* < 10^{-6}, 10^{-5}, 10^{-3}$ for $T_g = 10^2, 10^3, 10^4$ K, respectively. One can similarly gauge the unimportance of the collisional heating term by estimating the typical timescale for gas-grain collisions: $t_{\text{coll}} > 3 \times 10^5 \text{s}, 10^5 \text{s}, 3 \times 10^4 \text{s}$ for $T_g = 10^2, 10^3, 10^4$ K, respectively. These are long compared to the timescale for radiative heating. Thus, since the detailed gas properties have a non significant effect on our estimates, for the sake of simplicity, we assume $T_g = 10^3$ K throughout. We also adopt $f = 1$, corresponding to atomic hydrogen.

As an example, in Fig. 2, we present the dust temperature profile corresponding to the same systems shown in Fig. 1, where the UM-ND-20 model and standard grain size distribution has been assumed. Note that T_d increases significantly as $r \rightarrow 0$ because of the divergence of $f_{*,\nu}$ (Equ. 11). Therefore, in order to avoid numerical artefacts, we impose a lower cut-off for the radius at $r_{\text{cut}} =$

5 pc, as this is the typical size of a stellar cluster (e.g. Safranek-Shrader, Milosavljević & Bromm 2014). Furthermore, when T_d becomes sufficiently high, dust sublimates. The sublimation temperature depends on dust composition. Here, we again follow Ji, Frebel & Bromm (2014) and assume a sublimation temperature of 1500 K, typical of non-carbon grains (Schneider et al. 2006). In our model, central dust temperatures, at $r = r_{\text{cut}}$, increase with halo mass, and mainly depend on the size distribution of dust grains. For the standard distribution, the maximum T_d ranges from ≈ 70 K ($M_{\text{vir}} \approx 10^7 M_\odot$) to 1500 K ($M_{\text{vir}} \gtrsim 10^{12} M_\odot$), whereas for the shock size distribution, this range extends from ≈ 100 K ($M_{\text{vir}} \approx 10^7 M_\odot$) to 1500 K ($M_{\text{vir}} \gtrsim 10^{11} M_\odot$). Because of sublimation, dust is suppressed at $r \sim r_{\text{cut}}$ in more massive galaxies ($M_{\text{vir}} \gtrsim 10^{11-12} M_\odot$). As a baseline reference, for a typical atomic cooling halo ($M_{\text{vir}} \approx 10^8 M_\odot$), the maximum T_d lies between 100-120 K (standard size distribution) and 150-180 K (shock size distribution), depending on the dust composition. It is worth noting that, for carbon dust models, the sublimation temperature would increase to 2000 K, thus allowing higher central temperatures in more massive systems.

2.2.2 Dust emission

We compute the dust emissivity per unit mass (j_ν), at a given radius, by applying Kirchhoff's law for the estimated T_d profile:

$$j_\nu(T_d) = 4\pi\kappa_\nu B_\nu(T_d), \quad (13)$$

where B_ν is the Planck function. The total specific *dust* luminosity $L_{\nu,\text{em}}$ emitted by the system is obtained by integrating j_ν out to R_{vir} :

$$L_{\nu,\text{em}} = 4\pi \int_{r_{\text{cut}}}^{R_{\text{vir}}} \rho_d(r) j_\nu(r) r^2 dr. \quad (14)$$

The observed *dust* specific flux $f_{\nu,\text{obs}}$ originating from the model galaxy is then:

$$f_{\nu,\text{obs}} = (1+z) \frac{L_{\nu,\text{em}}}{4\pi d_L^2}, \quad (15)$$

where d_L is the luminosity distance to a source at redshift z .

In Figure 3, we show the emitted spectra (upper panel), together with the observed specific flux (lower panel), corresponding to the systems in Fig. 1 for the UM-ND-20 model and a standard size distribution for dust grains. Note that these spectra only represent *dust* emission; thus, they do not include the contribution from stellar sources. The dotted black curve, in the upper panel, depicts the frequency-dependent dust opacity, κ_ν , which has been re-scaled arbitrarily for the sake of comparison. The maximum emission is obtained at $\lambda \sim 50 \mu\text{m}$, corresponding to an observed wavelength of $\lambda_{\text{obs}} \sim 500 \mu\text{m}$. At longer wavelengths, the spectral slope is determined by the Rayleigh-Jeans tail of the distribution ($B_\nu \sim \nu^2$), modulated by the frequency-dependent dust opacity ($\kappa_\nu \sim \nu^{1.6}$, for the UM-ND-20 dust model). Thus, $f_{\nu,\text{obs}} \sim \nu_{\text{obs}}^{3.6}$ over this wavelength regime. At shorter wavelengths, the spectral shape traces the different absorption features associated with the given dust model (dotted black curve).

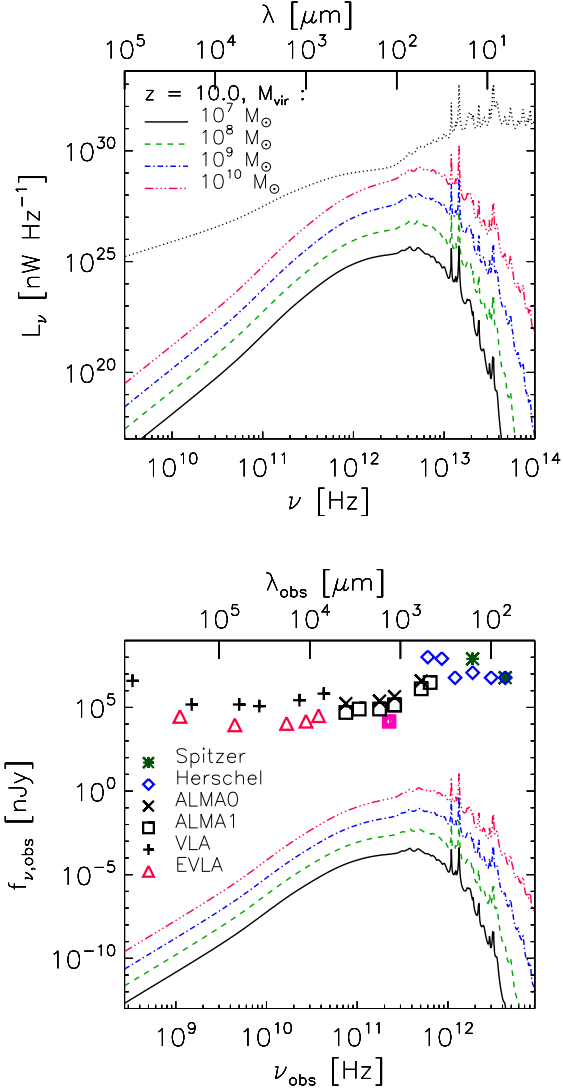


Figure 3. Dust re-emission spectra for individual sources. *Upper panel:* Rest-frame spectra for the same systems shown in Fig. 1, as indicated in the figure. The UM-ND-20 model and standard grain-size distribution has been assumed. The dotted black curve depicts the frequency-dependent dust opacity κ_ν , which has been re-scaled arbitrarily for the sake of comparison. *Lower panel:* Observed specific flux. Sensitivities of different instruments are shown with symbols as indicated in the figure (see text for details). The pink solid square represent one of the highest sensitivities achieved for ALMA maps in recent works ($\sim 10 \mu\text{Jy}/\text{beam}$, e.g. Carniani et al. 2015). Note that we are only dealing with *dust* emission in this work so that the contribution from stellar radiation to the total luminosity is not included in the calculations.

In the lower panel of Fig. 3, we additionally show the sensitivities of different observatories: Spitzer (green asterisks), Herschel (blue diamonds), ALMA (black X and squares for cycles 0 and 1 observations, respectively), the Very Large Array (VLA, black crosses), and the Expanded

Very Large Array (EVLA, red triangles).³ The pink solid square represent one of the highest sensitivities achieved for recent ALMA maps ($\sim 10 \mu\text{Jy}/\text{beam}$, e.g. Carniani et al. 2015). We see that the peak of the predicted dust emission is about four orders of magnitude below instrumental capabilities. Accordingly, point source sensitivities of current and near-future instruments are not sufficient to allow detection of dust emission from individual dwarf-size galaxies in the early Universe.

Confusion noise may affect the detection of luminous systems independently of instrument noise. We performed a rough estimate of confusion for our model galaxies following the procedure described in Section 4.1 in Kashlinsky et al. (2015). We obtained $\lesssim 10$ and $\lesssim 0.003$ beams/source for sources at $z < 20$ considering beam sizes of $0.7''$ and $37''$, respectively, consistent with the spatial resolution of ALMA compact configuration and Herschel at $\lambda \sim 500 \mu\text{m}$. Assuming that confusion intervenes when there are less than 50 beams/source (Condon 1974), all our sources are well within the confusion of ALMA compact configuration and Herschel instruments. However, for ALMA more extended 12-m array configurations, the finest angular resolutions for cycles 3 and 4 observations reach $0.04''$ - $0.032''$. We obtained that, in the latter case, model sources at $z > 13$ could overcome the confusion but, as we have shown, they would be too faint to be detected by ALMA.

As emission tends to significantly increase with mass, rare massive systems might be detectable, but are statistically difficult to find. In fact, by extrapolating our model to higher masses, we find that a halo mass of $M_{\text{vir}} \geq 10^{14} - 10^{15} M_\odot$ would be required to reach instrumental sensitivities. Such an object would have a *dust* luminosity of at least $L_{\text{em}} \sim 10^{12} - 10^{13} L_\odot$, consistent with the prototypical local ultra-luminous starburst galaxy Arp 220 ($\sim 10^{12} L_\odot$). Note, however, that at these high masses additional physical processes might have to be considered to correctly model dust emission, such as active galactic nuclei heating and the prolific dust generation after merger-induced starbursts.

Finally, we have assumed a conservative dust-to-metal ratio of $D = 0.005$. For larger D , the predicted dust emission would increase almost proportionally (Equ. 14), and the probability of observing these sources would be higher. As mentioned above, we show results for the UM-ND-20 dust model combined with a standard size distribution for dust grains. Other dust chemical compositions lead to similar findings. On the other hand, when using the shock size distribution, the predicted luminosities and fluxes increase by a factor $\lesssim 10$, where the exact boost depends on the dust chemistry (see also Sec. 3). Another assumption made here is a negligible contribution of carbon to the dust chemical composition. Schneider et al. (2006) compared opacities derived from a silicon-dominated dust model and one with similar contributions from silicon and carbon (their figures 1 and 2). We expect that our dust temperature profile does not exhibit significant variations if a moderate amount of car-

³ Sensitivities were taken from the *James Webb Space Telescope* website at <http://www.stsci.edu/jswt/science/sensitivity>, and correspond to the faintest flux for a point source that can be detected at $\text{SNR} = 10$ in a 10^4 s integration. We refer the reader to this web-page for further details.

bon were included: the steep temperature dependence of the dust cooling rate (Equ. 6) implies that opacity differences between models could be compensated by slight variations in T_d . However, at a given T_d , dust emissivities would be a factor of a few higher if we had adopted the Schneider et al. (2006) model that includes comparable amounts of silicon and carbon. Thus, a carbon-based model combined with a shock size distribution could increase the dust emission by a factor of ~ 10 , which still remains below instrumental capabilities, but a more detailed analysis is beyond the scope of the present paper.

It is worth mentioning that observations by Leiton et al. (2015) suggest that the main contributors to the EBL in all Herschel bands seem to be distant siblings of the Milky Way ($z \sim 1.0$ for $\lambda < 300\mu\text{m}$) with a stellar mass of $M_* \sim 9 \times 10^{10} M_\odot$. Also, Viero et al. (2013) suggest that the EBL is dominated by systems with $M_* \sim 10^{9.5-11} M_\odot$, and that the sources associated with wavelengths below and above $200\mu\text{m}$ are located at $z < 1$ and $1 < z < 2$, respectively. The low fluxes predicted by our models for individual primeval dust sources are consistent with these empirical constraints.

In the following section, we analyse the possibility of detecting signatures of integrated dust emission by studying the contribution of model galaxies to the EBL.

3 THE COSMIC FIR BACKGROUND

In order to estimate the contribution of the first galaxies to the FIR/sub-mm cosmic background, we combine the Sheth-Tormen mass function (Sheth, Mo & Tormen 2001) with our idealized models for individual sources in Sec. 2. As explained above, our models allow us to estimate the dust emission from primeval systems, once their properties are specified, such as their stellar, gas and dust distributions.

For sources located in a given redshift range $[z_{\min}, z_{\max}]$, the specific intensity contributed to the cosmic background at observed frequency ν_{obs} is given by:

$$I_\nu(\nu_{\text{obs}}) = \frac{c}{4\pi} \int_{z_{\min}}^{z_{\max}} \epsilon_\nu(\nu, z) \left| \frac{dt}{dz} \right| dz \quad (16)$$

where $\epsilon_\nu(\nu, z)$ is the specific luminosity per comoving volume element at redshift z and $\nu = \nu_{\text{obs}}(1+z)$ is the frequency at the rest frame of the source. Standard cosmology gives the expression:

$$\left| \frac{dt}{dz} \right|^{-1} = H_0 (1+z) [(1+z)^2(1+\Omega_m z) - z(2+z)\Omega_\Lambda]^{1/2} \quad (17)$$

We estimate $\epsilon_\nu(\nu, z)$, associated to dust emission, by combining the Sheth-Tormen mass function $n_{\text{ST}}(M_{\text{vir}}, z)$ ⁴ with the specific *dust* luminosities $L_\nu(M_{\text{vir}}, z)$ obtained by our idealized models:

$$\epsilon_\nu(\nu, z) = \int_{M_{\min}}^{M_{\max}} L_{\nu, \text{em}}(M_{\text{vir}}, z) n_{\text{ST}}(M_{\text{vir}}, z) dM_{\text{vir}} \quad (18)$$

⁴ The Sheth-Tormen formalism assumes ellipsoidal instead of spherical collapse and provides a better fit to simulations than the Press-Schechter (PS) formalism. The PS mass function underpredicts the abundance of haloes at high redshifts.

We here consider sources with typical masses and redshifts associated with first galactic systems: $M_{\text{vir}} \geq 10^7 M_\odot$ and $z \in [7, 20]$.

In Figure 4, we present the far-IR/sub-mm cosmic background predicted by our model assuming different dust compositions and grain size distributions. Dust emission from the first galaxies contributes most significantly to the EBL at $\lambda_{\text{obs}} \approx 100-1000\mu\text{m}$, exhibiting a peak at $\sim 500\mu\text{m}$. The spectral slope at longer wavelengths is given by the Rayleigh-Jeans law ($\sim \nu^2$) combined with the frequency-dependent dust opacity ($\kappa_\nu \sim \nu^n$, with n ranging from 1.0 to 1.8, depending on the dust model). Hence, in the long-wavelength regime, $\nu_{\text{obs}} I_\nu \propto \nu_{\text{obs}}^m$, with m between 4.0 and 4.8. At shorter wavelengths, the spectral shape traces the different features associated with the different dust opacities. These spectral features can also be discerned in Fig. 3, but in Fig. 4 they are smoothed and amplified because of the cumulative effect of sources contributing from different z (Equ. 16). For example, the spectral break at $\lambda_{\text{obs}} \approx 200\mu\text{m}$ in Fig. 4 corresponds to the cumulative, redshifted feature in κ_ν at $\nu \sim 10^{13}$ Hz (see Fig. 3, upper panel).

It is evident that the dust chemical composition does not significantly affect the main trends of the background radiation. On the other hand, changing the size distribution of dust grains seems to be more significant. In the case of the shock size distribution, the predicted background is around one order of magnitude higher than that corresponding to the standard size distribution. The absolute maximum intensities are $\sim 10^{-4} \text{ nW m}^{-2} \text{ sr}^{-1}$ and $\sim 10^{-3} \text{ nW m}^{-2} \text{ sr}^{-1}$ for the standard and shock size distributions, respectively.

The light-green lines and black circles in Fig. 4 show absolute measurements of, and limits on, the extragalactic background light taken from tables 3 – 5 in Dwek & Krennrich (2013), based on data obtained by different methods with an array of satellites, balloon-experiments, and ground-based observatories. At $\lambda_{\text{obs}} = 65$ and $90 \mu\text{m}$, data from the Akari infrared imaging satellite (ASTRO-F) has been used (Matsuura et al. 2011). Measurements from the Diffuse Infrared Background Experiment (DIRBE) on board the COsmic Background Explorer (COBE) satellite are shown at $\lambda_{\text{obs}} = 60 \mu\text{m}$ (Finkbeiner, Davis & Schlegel 2000), $100 \mu\text{m}$ (Hauser et al. 1998) and $140 \mu\text{m}$ (Hauser et al. 1998; Schlegel, Finkbeiner & Davis 1998). Results obtained by Fixsen et al. (1998) with COBE's Far Infrared Absolute Photometer (FIRAS) Pass 4 are plotted at $\lambda_{\text{obs}} = 140, 160, 240, 250, 350, 500$ and $850 \mu\text{m}$. The solid light-green line corresponds to the analytical fit to the spectrum given by Fixsen et al. (1998), while the dashed light-green line denotes the tentative background derived by Puget et al. (1996) from COBE/FIRAS Pass 3. In addition, we perform a rough estimation of the average source-subtracted EBL (red squares in Fig. 4) by removing the integrated galactic light (IGL) associated with foreground sources from the absolute EBL measurements. For this calculation, we used absolute measurements reported by Hauser et al. (1998) at $\lambda_{\text{obs}} = 100\mu\text{m}$ and Fixsen et al. (1998) at longer wavelengths. To estimate the IGL, we employed results derived by different authors from stacking analysis of astronomical images. Data at $\lambda_{\text{obs}} = 100 - 160 \mu\text{m}$ were obtained from the Photodetector Array Camera (PACS) on board Herschel (Dole et al. 2006; Berta et al. 2010). At

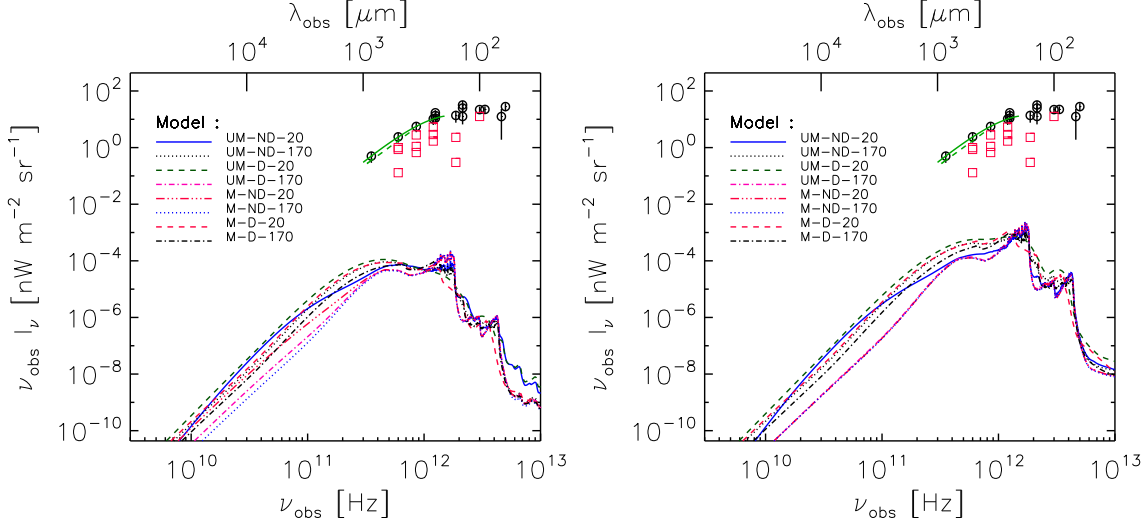


Figure 4. FIR/sub-mm-EBL from the first galaxies. We show the specific intensity, I_ν , of the cosmic background at observed frequency ν_{obs} , considering sources with $M_{\text{vir}} \geq 10^7 M_\odot$ located at $z \in [7, 20]$. *Left panel:* Results obtained by using the standard size distribution for dust grains. *Right panel:* Results for shock size distribution. Different dust models are considered as indicated in the figure. The light-green curves and circles with error bars depict observed measurements of the cosmic background derived from *Akari*, COBE/DIRBE and COBE/FIRAS instruments. Red squares represent an estimation of the CIB excess after removing the contribution of the IGL obtained by stacking analysis (see text for details).

$\lambda_{\text{obs}} > 200 \mu\text{m}$, we used measurements from the Balloon-borne Large-Aperture Submillimeter Telescope (BLAST; Marsden et al. 2009; Béthermin et al. 2010) and the Spectral and Photometric Imaging Receiver (SPIRE) on board Herschel (Béthermin et al. 2012). It is worth noting the large uncertainties ($\sim 1 - 10 \text{ nW m}^{-2} \text{ sr}^{-1}$) involved in the estimation of the source-subtracted EBL component, so caution should be taken when drawing conclusions from these data.

As can be seen, our model predictions fall below the measured absolute background by $\sim 3 - 4$ orders of magnitude, depending on the dust model. Moreover, our model spectrum is also below the average source-subtracted EBL by $\sim 2 - 3$ orders of magnitude. Thus, dust emission from the first galaxies might not contribute significantly to the observed absolute cosmic far-IR/sub-mm background. If this is the case, the bulk of the observed radiation in the FIR-EBL could be related to more evolved massive galaxies, located at lower z . It is worth mentioning that our model can roughly reproduce the Rayleigh-Jeans tail of the observed distribution. This suggests that the sources that contribute the bulk of the observed radiation should exhibit, on average, similar dust opacity trends as those assumed here.

To ascertain the nature of the sources contributing most significantly to the FIR-EBL, in Fig. 5, we analyse the luminosity density generated by model galaxies of different masses as a function of z . Results are shown for the UM-ND-20 dust model combined with a standard size distribution for dust grains. Other dust models produce similar trends. In the upper panels, we compare the luminosity density emitted by systems of different masses at a given z . It is evident that radiation from smaller galaxies ($M_{\text{vir}} \lesssim 10^{10} M_\odot$) dominates the EBL at $\lambda_{\text{obs}} \gtrsim 500 \mu\text{m}$ over the entire redshift range ($z = 7 - 20$). On the other hand, at $z \lesssim 10$, larger galaxies ($M_{\text{vir}} \gtrsim 10^{10} M_\odot$) become the dominant contributors to

the EBL at $\lambda_{\text{obs}} \lesssim 500 \mu\text{m}$. Similarly, in the lower panels of Fig. 5, we show the energy contribution from systems of a fixed mass at different z . We can see that massive galaxies ($M_{\text{vir}} \gtrsim 10^{10} M_\odot$) significantly contribute to the spectra only at $z \lesssim 10$, because of the increase in the number density of massive haloes at lower z . At the longest wavelengths ($\lambda \gtrsim 500 \mu\text{m}$), the main contributors to the EBL at $z \gtrsim 10$ are small galaxies ($M_{\text{vir}} \sim 10^{7-8} M_\odot$). To sum up, according to our model, the bulk of the FIR/sub-mm EBL originates in dwarf galaxies ($M_{\text{vir}} \lesssim 10^{10} M_\odot$) at $z = 7 - 20$, while radiation at shorter wavelengths can be associated with more massive systems at $z \sim 7$.

3.1 Sensitivity to variations of model parameters

In the following, we explore the sensitivity of our results to four of our most critical model parameters: the density profile, the dust-to-metal ratio D , the ISM metallicity Z_g and the star formation efficiency η .

With respect to the gas density, we have used an isothermal 1D profile (Equ. 1). In addition, we have tested the effects of using a Navarro-Frenk-White (NFW) density profile (Navarro, Frenk & White 1997) outside the core radius R_c :

$$\rho_g(r \geq R_c) = \frac{\rho_0}{\frac{r}{r_0} \left(1 + \frac{r}{r_0}\right)^2} \quad (19)$$

We have also implemented a profile of the Burkert (1995) form:

$$\rho_g(r) = \frac{\rho_0 r_0^3}{(r + r_0)(r^2 + r_0^2)} \quad (20)$$

In both cases, the parameters ρ_0 and r_0 were chosen to obtain similar central densities and total gas masses as

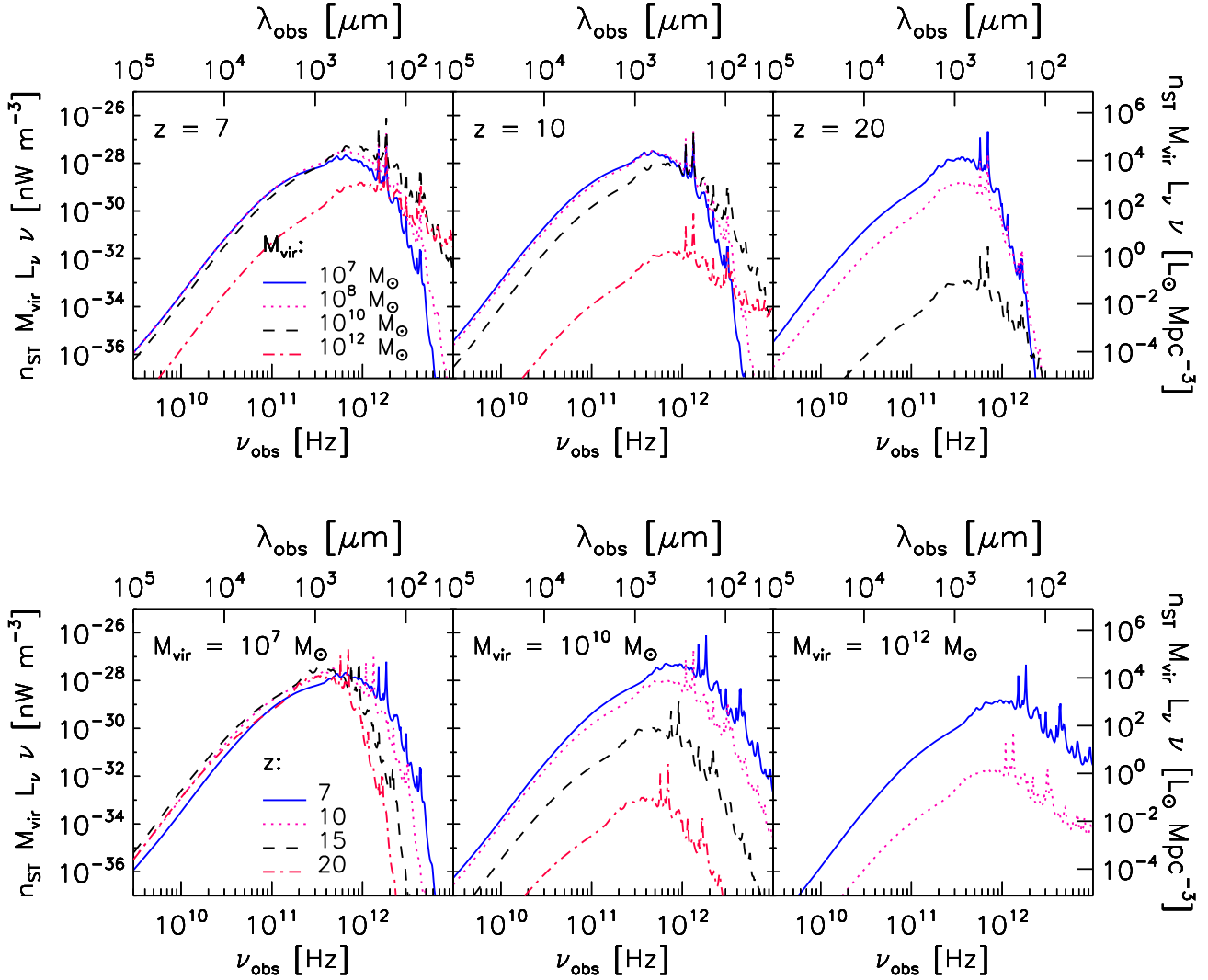


Figure 5. Energy emitted per unit time and comoving volume by model galaxies as a function of ν_{obs} . Upper panels compare the power emitted by systems of different masses at a fixed z , while lower panels show the energy contribution from systems of a given mass at different z . Left and right vertical axis show results in nW m^{-3} and $L_{\odot} \text{Mpc}^{-3}$, respectively. For the sake of clarity, results are shown for the UM-ND-20 dust model combined with a standard size distribution for dust grains. We have verified that other dust models produce similar trends.

those derived from Equ. 1. In comparison with the isothermal density profile, the implementation of the NFW profile at $r \geq R_c$ generates a mild decrease of mass at large radii and, consequently, an increase of it at intermediate radii. On the other hand, the use of the Burkert (1995) profile, instead of the isothermal one, results in a mild decrease of the core mass, a mild increase of the gas and dust masses at intermediate radii and a moderate decrease of mass density towards R_{vir} . We found that neither of these changes do significantly alter our previous results, because $H_d/H_* \ll 1$ and $\beta_{\text{esc}} \approx 1$. Thus, the T_d profile is not very sensitive to variations in ρ_d (Equ. 5).

We have also analysed the impact of increasing D . Following Cen & Kimm (2014), we considered cases with $D = 0.06$ and $D = 0.4$. Results are displayed in Fig. 6. As expected from Equ. 14, the radiation intensity increases

almost proportional to D . In particular, in the extreme case of $D = 0.4$, for both standard and shock grain-size distributions, the predicted background emission from high redshifts could reach 1% of the measured flux. Besides, for extremely high D , dust emission from first galaxies could reach $\sim 10\%$ of the source-subtracted EBL in the case of the standard size distribution for dust grains and almost $\sim 100\%$ if assuming the shock size distribution. In the lower panels of Fig. 6, we can see that the EBL also increases almost proportionally to Z_g (Equ. 14); thus, D and Z_g are degenerate quantities in our model. If Z_g could be determined by other means, the strong dependence of the emission on D suggests that EBL measurements at sub-mm wavelengths might provide important constraints on the amount of dust in the early Universe.

Finally, we explored the impact of increasing the star

formation efficiency to an extreme value of $\eta \sim 0.1$. As a higher η would result in an enhanced ISM metallicity, we also increased Z_g to 0.05, which is consistent with the closed-box model approximation $Z = -y \ln(1 - \eta)$, with y being the stellar yield. Although this approximation could not represent the real behaviour of these systems, it provides an upper limit for the predicted EBL. The obtained EBL spectrum is shown as a thick dashed black curve in Fig. 6, bottom panels. The model EBL is below the observed source-subtracted EBL by a factor of ~ 10 in the case of the standard size distribution for dust grains (left panel). On the other hand, for the shock size distribution (right panel), the model EBL obtained under the aforementioned extreme assumptions reaches the observed EBL excess.

In summary, an increase of D , Z_g and η from their fiducial values leads to a more important contribution of first galaxies to the FIR/sub-mm-EBL. Variations in D or Z_g produces similar changes in the EBL over our whole wavelength range while variations in η affects mainly the spectrum at $\lambda_{\text{obs}} < 1000 \mu\text{m}$. The source-subtracted EBL levels are only reached if extremely high values are assumed for these parameters. Mitchell-Wynne et al. (2015) found that the total intensity of radiation emerging from galaxies at $z > 6$ is $\log \nu I_\nu = -0.32 \pm 0.12$ at $1.6 \mu\text{m}$, with a dominant contribution from $z > 8$ sources. These authors constrained the cosmic luminosity density at $z > 8$ to be $\log \rho_{\text{UV}} = 27.4^{+0.2}_{-1.2} \text{ erg s}^{-1} \text{ Hz}^{-1} \text{ Mpc}^{-3}$, which is encouragingly similar to previous results derived by Kashlinsky et al. (2007) by using *Spitzer* data. These findings imply that a substantial fraction of the UV radiation at the epoch of reionization is associated with sources well below the sensitivity of current surveys. Here, we found that the contribution of these galaxies to the FIR-EBL would be even lower because of the low dust mass density in the early Universe. Hence, individual point-source detections of primordial dust sources are probably far beyond the capability of current instruments and upcoming facilities (Fig. 3). Our results are consistent with Fujimoto et al. (2016) who analysed faint 1.2 mm ALMA sources with a flux density of $\sim 0.01 - 1 \text{ mJy}$, concluding that the total integrated 1.2 mm flux corresponds to $104^{+27}_{-30} \%$ of the EBL, measured by the COBE satellite. These authors concluded that the dominant 1.2 mm EBL contributors might be sources with $\gtrsim 0.01 \text{ mJy}$.

4 THE NIR-EBL

It is well-known that roughly half of the stellar light ever emitted during the history of the Universe has been reprocessed by dust (Hauser & Dwek 2001). As the objective of the present work is the study of the FIR/sub-mm-EBL signatures associated with the first galaxies, our model is specially designed to describe the physics of dust emission. However, this model does not include the physical prescriptions required to predict the NIR-EBL, such as nebular emission or the reprocessing of Lyman- α photons by the intergalactic medium (e.g. Santos, Bromm & Kamionkowski 2002). Nevertheless, for the sake of comparison, we performed a rough estimation of the plausible contribution of our model galaxies to the NIR-EBL, assuming the same star formation rate densities as assumed in our FIR-EBL analysis. For this purpose, we implemented the simple formulation given in

Greif & Bromm (2006, section 3.2), but adapted to our own model parameters. The model links the ionizing photon production to the stellar mass inside halos:

$$I_{\text{NIR}} = \frac{hc}{4\pi m_H} \eta_{\text{ion}} \int_{z_{\text{min}}}^{z_{\text{max}}} \Psi_*(z) \left| \frac{dz}{dt} \right| dz, \quad (21)$$

where η_{ion} is the number of ionizing photons emitted per stellar baryon and $\Psi_*(z)$ is the star formation rate at a given z . We assumed $\eta_{\text{ion}} = 4 \times 10^3$, appropriate for Pop I/Pop II stars (see table 1 in Greif & Bromm 2006). For simplicity, we did not consider feedback effects when modelling the star formation rate. Thus,

$$\Psi_*(z) = \rho_m \frac{\Omega_b}{\Omega_M} \eta \left| \frac{dF_{\text{col}}(z)}{dz} \right| \left| \frac{dz}{dt} \right|, \quad (22)$$

where ρ_m is the total mass density of the background universe and $F_{\text{col}}(z)$ represents the collapsed fraction of mass available for star formation:

$$F_{\text{col}}(z) = \frac{1}{\rho_m} \int_{M_{\text{min}}}^{M_{\text{max}}} M_{\text{vir}} n_{\text{ST}}(M_{\text{vir}}, z) dM_{\text{vir}} \quad (23)$$

Note that Equ. 22 provides an upper limit for Ψ_* .

Using Equ. 21-23, we can obtain an estimate of the contribution of our model galaxies to the NIR-EBL, which can be compared to the FIR/sub-mm-EBL predicted by using Equ. 16. For our model parameters, we obtain $I_{\text{NIR}} \approx 3.4 \times 10^{-3} \text{ nW m}^{-2} \text{ sr}^{-1}$. This value is a factor of ~ 10 higher than our prediction for the FIR/sub-mm-EBL based on the standard size distribution for dust grains. However, the predicted I_{NIR} reaches a similar order of magnitude to our FIR/sub-mm-EBL when assuming a shock size distribution. It is worth mentioning that the simple model of Greif & Bromm (2006) combined with our model parameters is not able to reproduce the NIR-EBL excess of $\gtrsim 1 \text{ nW m}^{-2} \text{ sr}^{-1}$, inferred from the *Spitzer*/IRAC data (e.g. Kashlinsky et al. 2005). Even assuming a maximum star formation efficiency $\eta = 1$, the NIR-EBL associated with our galaxy population remains below $\sim 0.5 \text{ nW m}^{-2} \text{ sr}^{-1}$.

In Fig. 7, we compare the build-up of the CIB at NIR and FIR/sub-mm wavelengths associated with our model galaxies as a function of z . To obtain the distribution with z of the FIR/sub-mm-EBL, we replaced the integral over z in Equ. 16 with an integral over ν_{obs} for the interval $\lambda_{\text{obs}} = 100 - 1000 \mu\text{m}$. We can see that, if assuming a standard size distribution for dust grains, the FIR/sub-mm-EBL is a factor $\gtrsim 10$ below the NIR-EBL at all analysed z . On the other hand, for the shock size distribution, the ratio between the FIR/sub-mm and NIR EBL increases from ~ 0.03 at $z \sim 20$ to 0.5 at $z \sim 7$. As mentioned, a higher dust-to-metal ratio D or a higher ISM metallicity Z_g would lead to an increase of the FIR/sub-mm-EBL and, consequently, of the ratio between the FIR/sub-mm and NIR EBL.

Finally, according to a more recent and detailed analysis of Helgason et al. (2016), the contribution of galaxies at $z > 8$ to the NIR-EBL could reach $\sim 0.01 - 0.05 \text{ nW m}^{-2} \text{ sr}^{-1}$. If we compare these results with our findings regarding the FIR-EBL, the ratio between the FIR and NIR EBL at early times gives $\sim 0.002 - 0.01$ and $\sim 0.02 - 0.1$ for the standard and shock size distribution, respectively. Evidently, these values are significantly lower than the fraction of dust-reprocessed light inferred for lower z ($\sim 50\%$).

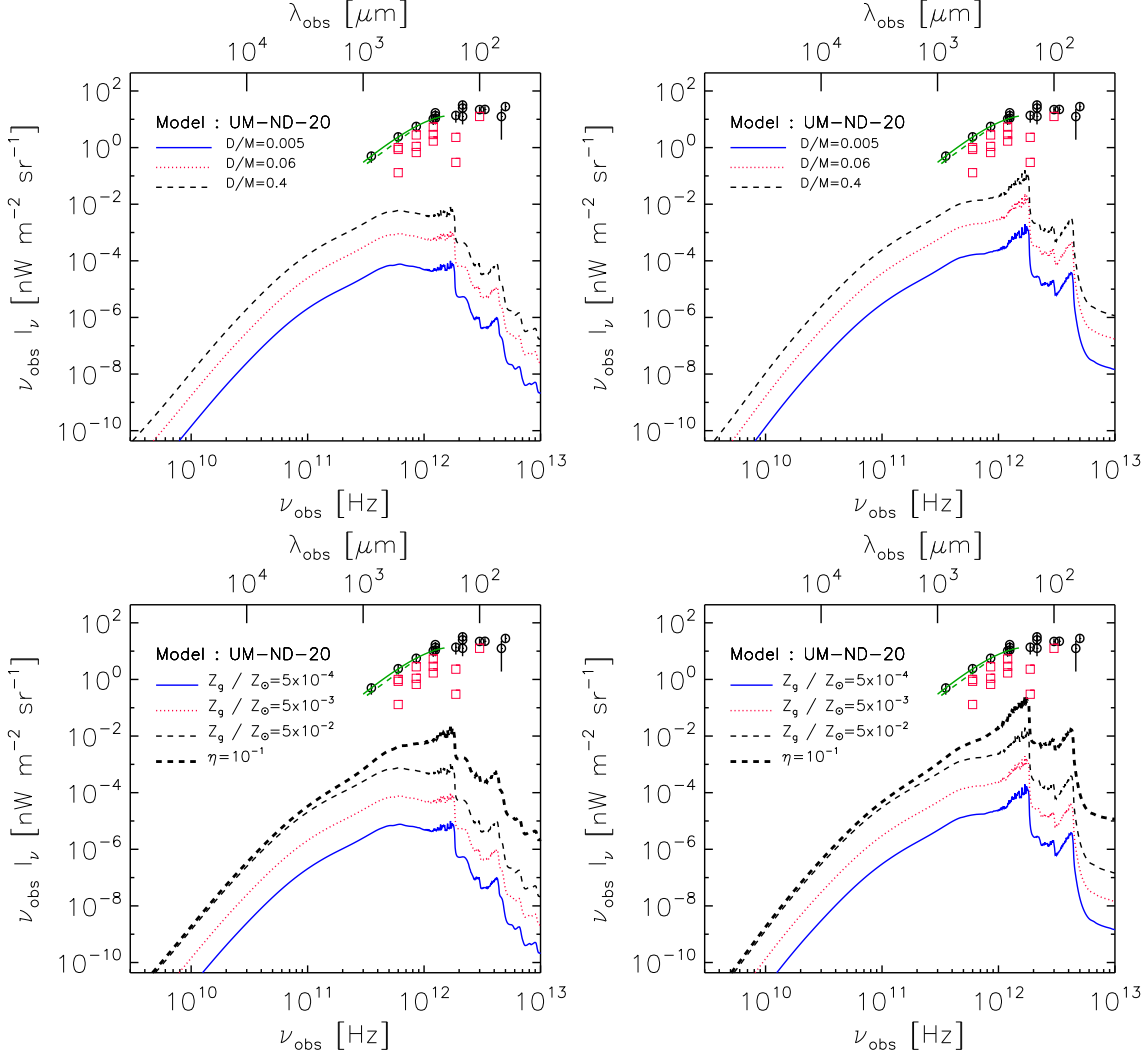


Figure 6. Similar to Fig. 4 but showing the effect of changing the dust-to-metal ratio (upper panels) and metallicity (lower panels) for a given dust model (UM-ND-20, in this case). In the lower panels, the thicker black dashed line corresponds to $Z_g = 10^{-2} Z_\odot$ and $\eta = 10^{-1}$. Left panels show results obtained by using the standard size distribution for dust grains, while right panels were generated by using the shock size distribution. The light-green curves and circles with error bars depict measurements of the cosmic background derived from *Akari*, COBE/DIRBE and COBE/FIRAS. Red squares represent an estimation of the CIB excess after removing the contribution of the IGL obtained by stacking analysis (see text for details).

5 SUMMARY AND CONCLUSIONS

We have analysed the contribution of high-redshift galactic systems to the FIR/sub-mm EBL by implementing an idealized analytical model for dust emission from the first galaxies. This model was then combined with the Sheth-Tormen halo mass function to estimate the observable cosmic background produced by those sources. We have considered different dust chemical compositions and grain size distributions.

Our main results can be summarized as follows:

- For typical primeval dwarf-size galaxies ($z \sim 10$, $M_{\text{vir}} \sim 10^8 M_\odot$), the peak of dust emission occurs at $\lambda_{\text{obs}} \sim 500 \mu\text{m}$. A standard size distribution for dust grains generates a maximum observed flux of $\sim 10^{-3} \text{ nJy}$ while, in the case of a

shock size distribution, observed fluxes are a factor $\lesssim 10$ higher. According to our model, the observed flux originating from a typical first galaxy would be below the instrumental capabilities of current and upcoming instruments. By extrapolating our models to higher masses, we find that a system of at least $10^{14} M_\odot$ is required to achieve detectability with the sensitivities of Herschel and ALMA. Also, increasing our conservative dust-to-metal ratio ($D = 5 \times 10^{-3}$) or ISM metallicity ($Z_g = 5 \times 10^{-3} Z_\odot$) would boost the resulting flux proportionally. A higher star formation efficiency than our fiducial value ($\eta = 0.01$) would also yield a higher flux, specially at $\lambda_{\text{obs}} < 1000 \mu\text{m}$.

- By integrating the cumulative dust emission from sources with $M_{\text{vir}} \geq 10^7 M_\odot$ located at $z = 7 - 20$, we obtained the FIR/sub-mm EBL emerging from the first galax-

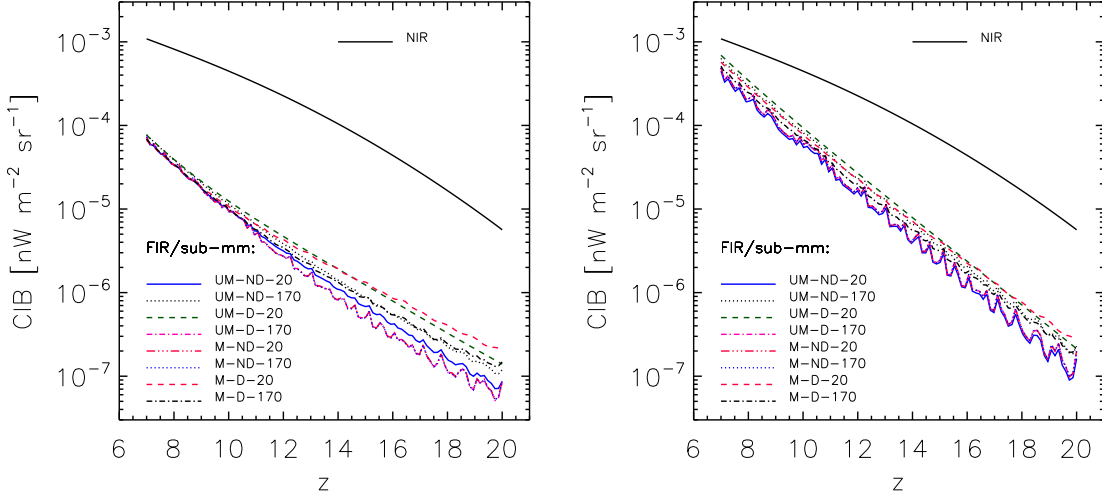


Figure 7. Contribution to the FIR/sub-mm-EBL of galaxy populations located at different z . Left and right panels show results derived from the standard and shock size distribution for dust grains, respectively. Findings for different dust chemical compositions are indicated with different line-styles, as indicated in the figure. The black solid lines depict the NIR-EBL obtained for our model galaxies by implementing the prescription given in Greif & Bromm (2006); see text for details.

ies. The model EBL peaks at $\lambda_{\text{obs}} \sim 500\mu\text{m}$ with an intensity of $\sim 10^{-4}$ and $\sim 10^{-3}\text{nW m}^{-2}\text{sr}^{-1}$ for the standard and shock size distribution of dust grains, respectively. Accordingly, dust emission from these systems would not contribute significantly to the measured cosmic FIR/sub-mm background, which exhibits values about $\sim 3 - 4$ orders of magnitude higher. The low fluxes at FIR/sub-mm wavelengths obtained for primeval galaxies are consistent with different observational constraints indicating that more massive and luminous galaxies at lower z might be the main contributors to the measured EBL (e.g. Viero et al. 2013; Leiton et al. 2015).

- The detailed chemical composition of dust has a non significant impact on the obtained FIR/sub-mm EBL, at least for the dust models studied here. In particular, in the Rayleigh-Jeans regime, the slope of the model EBL spectrum approaches the observed one. Thus, sources contributing to the observed EBL emission would exhibit similar dust opacity curves as those used here.

- By analysing the luminosity density as a function of the mass and redshift of model galaxies, we found that the bulk of the FIR/sub-mm EBL is associated with dwarf galaxies ($M_{\text{vir}} \lesssim 10^{10} M_{\odot}$) at $z = 7 - 20$, while more massive galaxies at $z \sim 7$ tend to contribute mostly to the background at shorter wavelengths.

- Because of the low ISM densities of model galaxies, our results seem to be robust against moderate variations in gas temperature or composition. Also, we obtained no significant variations in our results when changing from the isothermal to the NFW and Burkert gas density profiles. However, the model EBL exhibits a strong correlation with the dust-to-metal ratio D , increasing almost proportionally with it. Hence, measurements of the FIR/sub-mm EBL could provide important constraints on the amount of dust at early epochs.

- By implementing a simple scheme, we made a rough estimation of the plausible contribution of our model galaxies to the NIR-EBL. We obtained $I_{\text{NIR}} \approx 3 \times 10^{-3}\text{nW m}^{-2}\text{sr}^{-1}$, which agrees with the values predicted for the FIR/sub-mm-EBL when using a shock size distribution for dust grains. In the case of the standard size distribution, the predicted FIR/sub-mm flux is below I_{NIR} by a factor of ~ 10 . If we compare results from the more sophisticated NIR model by Helgason et al. (2016) with our findings regarding the FIR-EBL, the ratio between the FIR and NIR EBL at early times gives $\sim 0.002 - 0.01$ and $\sim 0.02 - 0.1$ for the standard and shock size distribution, respectively.

Finally, measurements of the EBL are affected by the presence of significant foregrounds at FIR/sub-mm wavelengths: zodiacal light and Galactic cirrus at $\lambda < 300\mu\text{m}$ and the cosmic microwave background at longer wavelengths. Thus, absolute flux measurements of the FIR-EBL constitutes a very challenging task. Although the low contribution to the net flux might prevent such absolute measurements of primordial dust emission, it might still be possible to obtain information about it by exploring the EBL angular power spectrum (Kashlinsky, Mather & Odenwald 1996; Kashlinsky et al. 1996; Kashlinsky & Odenwald 2000; Arendt et al. 2010; Mitchell-Wynne et al. 2015), which we will investigate in a separate paper. According to our model, these signatures should be detected at $\sim 500\mu\text{m}$, close to the peak of dust emission from primeval sources. The overall hope is to open up complementary windows into the different phases of the high-redshift star formation process, by matching state-of-the-art theoretical predictions to the powerful array of next-generation observational facilities.

ACKNOWLEDGEMENTS

We thank the referee of this paper for useful suggestions and comments that improved the manuscript. We thank Alexander Ji for providing tabulated dust opacities for the different dust models used here. This work makes use of the Yggdrasil code (Zackrisson et al. 2011), which adopts Starburst99 SSP models, based on Padova-AGB tracks (Leitherer et al. 1999; Vázquez & Leitherer 2005) for Population II stars. VB would like to thank the IAFE in Buenos Aires for its hospitality during the early stages of this work, and acknowledges support from NSF grant AST-1413501. MEDR is grateful to PICT-2015-3125 of ANPCyT (Argentina) and also to María Sanz and Guadalupe Lucia for their help and support.

REFERENCES

- Abel T., Bryan G. L., Norman M. L., 2002, *Science*, 295, 93
- Allende Prieto C., Lambert D. L., Asplund M., 2001, *ApJ*, 556, L63
- Arendt R. G., Kashlinsky A., Moseley S. H., Mather J., 2010, *ApJS*, 186, 10
- Asplund M., Grevesse N., Sauval A. J., 2005, in *Astronomical Society of the Pacific Conference Series*, Vol. 336, *Cosmic Abundances as Records of Stellar Evolution and Nucleosynthesis*, Barnes III T. G., Bash F. N., eds., p. 25
- Asplund M., Grevesse N., Sauval A. J., Scott P., 2009, *ARA&A*, 47, 481
- Barkana R., Loeb A., 2001, *Phys. Rep.*, 349, 125
- Beichman C. A., Helou G., 1991, *ApJ*, 370, L1
- Berta S. et al., 2010, *A&A*, 518, L30
- Béthermin M., Dole H., Cousin M., Bavouzet N., 2010, *A&A*, 516, A43
- Béthermin M. et al., 2012, *A&A*, 542, A58
- Bianchi S., Schneider R., 2007, *MNRAS*, 378, 973
- Binney J., Tremaine S., 2008, *Galactic Dynamics: Second Edition*. Princeton University Press
- Bromm V., 2013a, *Reports on Progress in Physics*, 76, 112901
- Bromm V., 2013b, *Asociacion Argentina de Astronomia La Plata Argentina Book Series*, 4, 3
- Bromm V., Coppi P. S., Larson R. B., 2002, *ApJ*, 564, 23
- Bromm V., Larson R. B., 2004, *ARA&A*, 42, 79
- Bromm V., Loeb A., 2003, *Nature*, 425, 812
- Bromm V., Yoshida N., 2011, *ARA&A*, 49, 373
- Bromm V., Yoshida N., Hernquist L., McKee C. F., 2009, *Nature*, 459, 49
- Burkert A., 1995, *ApJ*, 447, L25
- Cai Z.-Y. et al., 2013, *ApJ*, 768, 21
- Carniani S. et al., 2015, *A&A*, 584, A78
- Carr B. J., Bond J. R., Arnett W. D., 1984, *ApJ*, 277, 445
- Casey C. M., Narayanan D., Cooray A., 2014, *Phys. Rep.*, 541, 45
- Cen R., Kimm T., 2014, *ApJ*, 782, 32
- Cherchneff I., Dwek E., 2010, *ApJ*, 713, 1
- Chiaki G., Marassi S., Nozawa T., Yoshida N., Schneider R., Omukai K., Limongi M., Chieffi A., 2015, *MNRAS*, 446, 2659
- Condon J. J., 1974, *ApJ*, 188, 279
- Cooray A., Bock J. J., Keatin B., Lange A. E., Matsumoto T., 2004, *ApJ*, 606, 611
- Cooray A., Yoshida N., 2004, *MNRAS*, 351, L71
- Coppin K. et al., 2006, *MNRAS*, 372, 1621
- Couchman H. M. P., Rees M. J., 1986, *MNRAS*, 221, 53
- Dole H. et al., 2006, *A&A*, 451, 417
- Dopcke G., Glover S. C. O., Clark P. C., Klessen R. S., 2013, *ApJ*, 766, 103
- Draine B. T., 2011, *Physics of the Interstellar and Inter-galactic Medium*
- Draine B. T., Li A., 2001, *ApJ*, 551, 807
- Dwek E. et al., 1998, *ApJ*, 508, 106
- Dwek E., Krennrich F., 2013, *Astroparticle Physics*, 43, 112
- Eales S., Lilly S., Webb T., Dunne L., Gear W., Clements D., Yun M., 2000, *AJ*, 120, 2244
- Ferland G. J., Korista K. T., Verner D. A., Ferguson J. W., Kingdon J. B., Verner E. M., 1998, *PASP*, 110, 761
- Finkbeiner D. P., Davis M., Schlegel D. J., 2000, *ApJ*, 544, 81
- Fixsen D. J., Dwek E., Mather J. C., Bennett C. L., Shafer R. A., 1998, *ApJ*, 508, 123
- Frebel A., Johnson J. L., Bromm V., 2007, *MNRAS*, 380, L40
- Fujimoto S., Ouchi M., Ono Y., Shibuya T., Ishigaki M., Nagai H., Momose R., 2016, *ApJS*, 222, 1
- Furlanetto S. R., Loeb A., 2003, *ApJ*, 588, 18
- Gall C., Hjorth J., Andersen A. C., 2011, *A&A Rev.*, 19, 43
- Greif T. H., Bromm V., 2006, *MNRAS*, 373, 128
- Greif T. H., Springel V., White S. D. M., Glover S. C. O., Clark P. C., Smith R. J., Klessen R. S., Bromm V., 2011, *ApJ*, 737, 75
- Haiman Z., Thoul A. A., Loeb A., 1996, *ApJ*, 464, 523
- Hatsukade B., Ohta K., Seko A., Yabe K., Akiyama M., 2013, *ApJ*, 769, L27
- Hauser M. G. et al., 1998, *ApJ*, 508, 25
- Hauser M. G., Dwek E., 2001, *ARA&A*, 39, 249
- Helgason K., Ricotti M., Kashlinsky A., Bromm V., 2016, *MNRAS*, 455, 282
- Hollenbach D., McKee C. F., 1979, *ApJS*, 41, 555
- Ji A. P., Frebel A., Bromm V., 2014, *ApJ*, 782, 95
- Karlsson T., Bromm V., Bland-Hawthorn J., 2013, *Reviews of Modern Physics*, 85, 809
- Kashlinsky A., 2005, *Phys. Rep.*, 409, 361
- Kashlinsky A., Arendt R., Gardner J. P., Mather J. C., Moseley S. H., 2004, *ApJ*, 608, 1
- Kashlinsky A., Arendt R. G., Mather J., Moseley S. H., 2005, *Nature*, 438, 45
- Kashlinsky A., Arendt R. G., Mather J., Moseley S. H., 2007, *ApJ*, 654, L1
- Kashlinsky A., Mather J. C., Helgason K., Arendt R. G., Bromm V., Moseley S. H., 2015, *ApJ*, 804, 99
- Kashlinsky A., Mather J. C., Odenwald S., 1996, *ApJ*, 473, L9
- Kashlinsky A., Mather J. C., Odenwald S., Hauser M. G., 1996, *ApJ*, 470, 681
- Kashlinsky A., Odenwald S., 2000, *ApJ*, 528, 74
- Kashlinsky A., Odenwald S., Mather J., Skrutskie M. F., Cutri R. M., 2002, *ApJ*, 579, L53
- Kaufman M., 1976, *Ap&SS*, 40
- Kormendy J., Fisher D. B., Cornell M. E., Bender R., 2009, *ApJS*, 182, 216
- Larson R. B., 1969, *MNRAS*, 145, 405
- Leitherer C. et al., 1999, *ApJS*, 123, 3

- Leiton R. et al., 2015, *A&A*, 579, A93
- Loeb A., 2010, *How Did the First Stars and Galaxies Form?*
Princeton Univ. Press, Princeton
- Loeb A., Haiman Z., 1997, *ApJ*, 490, 571
- Low F. J., Tucker W. H., 1968, *Physical Review Letters*,
21, 1538
- Magliocchetti M., Salvaterra R., Ferrara A., 2003, *MNRAS*,
342, L25
- Marsden G. et al., 2009, *ApJ*, 707, 1729
- Matsuura S. et al., 2011, *ApJ*, 737, 2
- Mayer M., Duschl W. J., 2005, *MNRAS*, 358, 614
- Mitchell-Wynne K. et al., 2015, *Nature Communications*,
6, 7945
- Navarro J. F., Frenk C. S., White S. D. M., 1997, *ApJ*, 490,
493
- Nozawa T., Kozasa T., 2013, *ApJ*, 776, 24
- Omukai K., 2000, *ApJ*, 534, 809
- Omukai K., Hosokawa T., Yoshida N., 2010, *ApJ*, 722, 1793
- Ono Y., Ouchi M., Kurono Y., Momose R., 2014, *ApJ*, 795,
5
- Planck Collaboration et al., 2014, *A&A*, 571, A16
- Pollack J. B., Hollenbach D., Beckwith S., Simonelli D. P.,
Roush T., Fong W., 1994, *ApJ*, 421, 615
- Puget J.-L., Abergel A., Bernard J.-P., Boulanger F., Bur-
ton W. B., Desert F.-X., Hartmann D., 1996, *A&A*, 308,
L5
- Safronek-Shrader C., Bromm V., Milosavljević M., 2010,
ApJ, 723, 1568
- Safronek-Shrader C., Milosavljević M., Bromm V., 2014,
MNRAS, 438, 1669
- Salvaterra R., Ferrara A., 2003, *MNRAS*, 339, 973
- Salvaterra R., Ferrara A., 2006, *MNRAS*, 367, L11
- Santos M. R., Bromm V., Kamionkowski M., 2002, *MN-
RAS*, 336, 1082
- Schlegel D. J., Finkbeiner D. P., Davis M., 1998, *ApJ*, 500,
525
- Schneider R., Ferrara A., Salvaterra R., 2004, *MNRAS*,
351, 1379
- Schneider R., Omukai K., Inoue A. K., Ferrara A., 2006,
MNRAS, 369, 1437
- Sheth R. K., Mo H. J., Tormen G., 2001, *MNRAS*, 323, 1
- Smith A., Safronek-Shrader C., Bromm V., Milosavljević
M., 2015, *MNRAS*, 449, 4336
- Stacy A., Greif T. H., Bromm V., 2010, *MNRAS*, 403, 45
- Tegmark M., Silk J., Rees M. J., Blanchard A., Abel T.,
Palla F., 1997, *ApJ*, 474, 1
- Vázquez G. A., Leitherer C., 2005, *ApJ*, 621, 695
- Viero M. P. et al., 2013, *ApJ*, 779, 32
- Weiß A. et al., 2009, *ApJ*, 707, 1201
- Wilson G. W. et al., 2008, *MNRAS*, 386, 807
- Yoshida N., Abel T., Hernquist L., Sugiyama N., 2003,
ApJ, 592, 645
- Yoshida N., Bromm V., Hernquist L., 2004, *ApJ*, 605, 579
- Zackrisson E., Rydberg C.-E., Schaerer D., Östlin G., Tuli
M., 2011, *ApJ*, 740, 13